



# Spin transition of ferric iron in the NAL phase: Implications for the seismic heterogeneities of subducted slabs in the lower mantle



Ye Wu<sup>a,b</sup>, Xiang Wu<sup>a,\*</sup>, Jung-Fu Lin<sup>b,c,\*\*</sup>, Catherine A. McCammon<sup>d</sup>, Yuming Xiao<sup>e</sup>, Paul Chow<sup>e</sup>, Vitali B. Prakapenka<sup>f</sup>, Takashi Yoshino<sup>g</sup>, Shuangmeng Zhai<sup>h</sup>, Shan Qin<sup>a</sup>

<sup>a</sup> Key Laboratory of Orogenic Belts and Crustal Evolution, MOE, Peking University and School of Earth and Space Sciences, Peking University, Beijing 100871, China

<sup>b</sup> Department of Geological Sciences, Jackson School of Geosciences, The University of Texas at Austin, Austin, TX 78712, USA

<sup>c</sup> Center for High Pressure Science and Technology Advanced Research (HPSTAR), Shanghai 201900, China

<sup>d</sup> Bayerisches Geoinstitut, Universität Bayreuth, D-95440 Bayreuth, Germany

<sup>e</sup> HPCAT, Geophysical Laboratory, Carnegie Institution of Washington, Argonne, IL 60439, USA

<sup>f</sup> GeoSoilEnviroCARS, The University of Chicago, Chicago, IL 60637, USA

<sup>g</sup> Institute for Study of the Earth's Interior, Okayama University, Misasa, Tottori 682-0193, Japan

<sup>h</sup> Key Laboratory of High-temperature and High-pressure Study of the Earth's Interior, Institute of Geochemistry, Chinese Academy of Sciences, Guiyang 550002, China

## ARTICLE INFO

### Article history:

Received 13 July 2015

Received in revised form 14 October 2015

Accepted 10 November 2015

Available online 2 December 2015

Editor: J. Brodholt

### Keywords:

NAL phase

spin transition

subducted slabs

lower mantle

seismic heterogeneities

## ABSTRACT

Al-rich phases (NAL: new hexagonal aluminous phase and CF: calcium–ferrite phase) are believed to constitute 10–30 wt% of subducted mid-ocean ridge basalt (MORB) in the Earth's lower mantle. In order to understand the effects of iron on compressibility and elastic properties of the NAL phase, we have studied two single-crystal samples (Fe-free  $\text{Na}_{1.14}\text{Mg}_{1.83}\text{Al}_{4.74}\text{Si}_{1.23}\text{O}_{12}$  and Fe-bearing  $\text{Na}_{0.71}\text{Mg}_{2.05}\text{Al}_{4.62}\text{Si}_{1.16}\text{Fe}^{2+}_{0.09}\text{Fe}^{3+}_{0.17}\text{O}_{12}$ ) using synchrotron nuclear forward scattering (NFS) and X-ray diffraction (XRD) combined with diamond anvil cells up to 86 GPa at room temperature. A pressure-induced high-spin (HS) to low-spin (LS) transition of the octahedral  $\text{Fe}^{3+}$  in the Fe-bearing NAL is observed at approximately 30 GPa by NFS. Compared to the Fe-free NAL, the Fe-bearing NAL undergoes a volume reduction of 1.0% ( $\sim 1.2 \text{ \AA}^3$ ) at 33–47 GPa as supported by XRD, which is associated with the spin transition of the octahedral  $\text{Fe}^{3+}$ . The fits of Birch–Murnaghan equation of state (B–M EoS) to  $P$ – $V$  data yield unit-cell volume at zero pressure  $V_0 = 183.1(1) \text{ \AA}^3$  and isothermal bulk modulus  $K_{T0} = 233(6) \text{ GPa}$  with a pressure derivative  $K'_{T0} = 3.7(2)$  for the Fe-free NAL;  $V_{0\text{-HS}} = 184.76(6) \text{ \AA}^3$  and  $K_{T0\text{-HS}} = 238(1) \text{ GPa}$  with  $K'_{T0\text{-HS}} = 4$  (fixed) for the Fe-bearing NAL. The bulk sound velocities ( $V_\phi$ ) of the Fe-free and Fe-bearing NAL phase are approximately 6% larger than those of Al, Fe-bearing bridgmanite and calcium silicate perovskite in the lower mantle, except for the spin transition region where a notable softening of  $V_\phi$  with a maximum reduction of 9.4% occurs in the Fe-bearing NAL at 41 GPa. Considering the high volume proportion of the NAL phase in subducted MORB, the distinct elastic properties of the Fe-bearing NAL phase across the spin transition reported here may provide an alternative plausible explanation for the observed seismic heterogeneities of subducted slabs in the lower mantle at depths below 1200 km.

© 2015 Elsevier B.V. All rights reserved.

## 1. Introduction

Mid-ocean ridge basalt (MORB) is generated by means of partial melting of the upper-mantle peridotite along mid-ocean ridges, enriching aluminum, iron, and other incompatible elements (Green et al., 1979; Hofmann, 1997). The MORB, in turn, can be trans-

ported back into the Earth's interior via subduction of slab materials at plate convergence regions, supplying the mantle with chemically distinct and heterogeneous materials. Due to differences in temperature, chemical composition and mineral constituent between subducted slabs and normal mantle peridotite, subducted slabs exhibit higher seismic velocities than peridotite in the Earth's mantle (Bina and Helffrich, 2014; Fukao et al., 2009). Furthermore, seismic anomalies observed in the mantle, such as seismic scatterers and mid-lower mantle discontinuities, are generally suggested to be related to subducted slabs (Kaneshima, 2013; Kawakatsu and Niu, 1994). Therefore, in order to have a better un-

\* Corresponding author.

\*\* Corresponding author at: Department of Geological Sciences, Jackson School of Geosciences, The University of Texas at Austin, Austin, TX 78712, USA.

E-mail addresses: xiang.wu@pku.edu.cn (X. Wu), afu@jsg.utexas.edu (J.-F. Lin).

derstanding of the geochemical and geophysical properties of the deep Earth, it is essential to have a thorough understanding of the thermal elastic properties of the minerals potentially present in the slabs.

MORB assemblage is generally expected to have distinct chemical compositions that contain more aluminum than the bulk mantle (Green et al., 1979; Sun, 1982). These basaltic materials have been reported to transform into an assemblage of magnesium silicate perovskite (Mg–Pv, named bridgmanite), calcium silicate perovskite (Ca–Pv), stishovite, and aluminous-rich phases in the lower mantle (Hirose et al., 2005; Irifune and Ringwood, 1993; Ohta et al., 2008; Ricolleau et al., 2010). An aluminous phase with calcium-ferrite (CF) structure (*Pbnm*,  $Z = 4$ ) was found in subducted oceanic crust at pressures above 25 GPa and temperatures above 1200 °C (Irifune and Ringwood, 1993). Following this pioneering work, another aluminous phase, named “new hexagonal aluminous phase (NAL)”, was subsequently observed in the garnet-to-perovskite transformation and the  $\text{MgAl}_2\text{O}_4$ – $\text{CaAl}_2\text{O}_4$  system at relevant conditions of the lower mantle (Akaogi et al., 1999; Miyajima et al., 1999). Recently, studies on mineral inclusions in diamonds from Juina-5 kimberlite indicate that these mineral inclusions have compositions consistent with the phase assemblage expected to crystallize from basaltic materials at lower-mantle conditions, comprising of Mg–Pv, Ca–Pv, NAL, CF, and  $\text{SiO}_2$  phases (Walter et al., 2011). These results provide direct petrological evidence for the existence of the NAL and CF phases in subducted MORB assemblage in the lower mantle. NAL and CF phases therefore have been considered as the main hosts of aluminum accounting for 10~30 wt% of the subducted basalt in the lower mantle (Ricolleau et al., 2010).

The NAL phase with a chemical formula of  $\text{AB}_2\text{C}_6\text{O}_{12}$  has a hexagonal crystal structure with the space group of  $P6_3/m$ . (Fig. S1) (Miura et al., 2000). The A site, located on a tunnel with a hexagonal cross-section in the projection of the *c*-axis direction, is partially occupied by a large monovalent or divalent cation ( $\text{Na}^+$ ,  $\text{K}^+$ , or  $\text{Ca}^{2+}$ ). The B site has a di-trigonal cross-section and is occupied by a smaller cation ( $\text{Mg}^{2+}$  or  $\text{Fe}^{2+}$ ) to form a trigonal prismatic coordination polyhedron with surrounding oxygen atoms. The C site, an octahedral site, is occupied by  $\text{Al}^{3+}$ ,  $\text{Fe}^{3+}$ , and/or  $\text{Si}^{4+}$ . Edge-sharing  $\text{CO}_6$  octahedra are arranged along the *c*-axis direction to form a chain framework structure. By sharing corners in the *ab* plane, three edge-sharing double chains form two kinds of tunnels for A and B sites, respectively (Miura et al., 2000). The CF phase with a chemical formula of  $\text{B}_3\text{C}_6\text{O}_{12}$  has a chain framework structure along the *c*-axis direction similar to the NAL phase, but it only forms one kind of tunnel with a di-trigonal cross-section in the *ab* plane for the B-site cation (Yamada et al., 1983).

The high amount of Al-rich phases in the subducted MORB assemblage has motivated extensive studies of their phase stabilities and physical properties as they can relate to the properties of subducted slabs in the lower mantle (Dai et al., 2013; Guignot and Andraut, 2004; Imada et al., 2011; Kawai and Tsuchiya, 2012; Ono et al., 2009). High pressure–temperature (P–T) X-ray diffraction (XRD) and transmission electron microscopy studies on a natural MORB assemblage indicate that the NAL and CF phases coexist up to ~50 GPa, beyond which only the CF phase is observed (Ricolleau et al., 2010), and results on phase relations of the  $\text{NaAlSiO}_4$ – $\text{MgAl}_2\text{O}_4$  system show that the CF phase is identified as the high pressure form of the NAL phase (Imada et al., 2011; Ono et al., 2009). Studies on the MORB assemblage further show that the NAL phase is more enriched in potassium than the coexisting CF phase such that the NAL phase is stabilized to higher pressures (Guignot and Andraut, 2004; Kato et al., 2013). On the other hand, Brillouin light scattering studies on polycrystalline samples and theoretical calculations have suggested that the change in the

shear wave anisotropy across the NAL to CF phase transition is significant enough to be seismically detectable (Dai et al., 2013; Kawai and Tsuchiya, 2012), affecting our understanding of seismic signatures of the subducted slabs in the lower mantle.

The NAL and CF phases contain a certain amount of iron (Ricolleau et al., 2010), which can potentially affect physical and chemical properties of the host minerals at extreme P–T conditions. The spin and valence states of iron in various crystallographic sites of the candidate lower-mantle phases have been investigated using synchrotron X-ray and spectroscopic techniques as well as first-principle calculations (Lin et al., 2013 and references therein). Electronic high-spin (HS) to low-spin (LS) transitions of iron have been reported to occur in a number of candidate mantle minerals, including ferropericlase, bridgmanite, ferromagnesite, and Phase D (Chang et al., 2013; Lin et al., 2012, 2005; Liu et al., 2014). In ferropericlase ( $\text{Mg,FeO}$ ), octahedral  $\text{Fe}^{2+}$  undergoes a spin transition at approximately 40 to 50 GPa (Lin et al., 2005). In  $\text{ABO}_3$ -type bridgmanite,  $\text{Fe}^{2+}$  predominantly occupies the pseudo-dodecahedral A site, whereas  $\text{Fe}^{3+}$  occupies both the A and octahedral B sites (Lin et al., 2012). The current consensus for the spin and valence states of iron in bridgmanite is that the octahedral  $\text{Fe}^{3+}$  undergoes a spin transition at pressures of the uppermost lower mantle, while  $\text{Fe}^{2+}$  and  $\text{Fe}^{3+}$  in the pseudo-dodecahedral site remain in the high-spin state throughout the entire lower mantle (Lin et al., 2013). Studies on the aforementioned Al-rich phases so far have been mostly focused on their phase stabilities and equation of state (EoS) parameters, while the influence of iron on elastic properties has yet to be investigated. Since the NAL phase likely contains up to 12 mol% iron (Ricolleau et al., 2010), the valence and spin states of iron in the NAL phase can potentially affect its elasticity which in turn can affect our understanding of the mineral physics of the MORB assemblage in the lower mantle (Lin et al., 2013).

Here we have studied two single-crystal samples of the NAL phase, Fe-free and Fe-bearing, to investigate the spin and valence states of iron in the NAL phase and the effects of iron on EoS parameters of the NAL phase using nuclear forward scattering (NFS) and XRD in conjunction with diamond anvil cells (DAC). A spin transition in the octahedral  $\text{Fe}^{3+}$  of the Fe-bearing NAL phase is observed at approximately 30 GPa from the NFS, and it can be associated with changes in the lattice parameters evaluated from the XRD measurements. These results are compared to other candidate minerals in the MORB assemblage and applied to understand their influences on the seismic profiles of the lower mantle.

## 2. Experimental methods

### 2.1. Sample synthesis and characterization

Single crystals of the Fe-free and Fe-bearing NAL phases were synthesized using the 5000-ton Kawai-type multi-anvil apparatus (USSA-5000) at the Institute for Study of the Earth’s Interior (ISEI), Okayama University at Misasa.  $\text{NaAlSiO}_4$  (nepheline,  $P6_3$ ) was firstly synthesized by heating stoichiometric mixtures of  $\text{NaCO}_3$ ,  $\text{Al}_2\text{O}_3$  and  $\text{SiO}_2$  at 1200 °C for 12 hrs. Subsequently, a mixture of  $\text{NaAlSiO}_4$ ,  $\text{MgO}$  and  $\text{Al}_2\text{O}_3$  in a molar ratio of 0.4 : 0.6 : 0.6 was used as the starting materials for synthesizing the Fe-free NAL phase. 2 wt%  $\text{H}_2\text{O}$  in the form of  $\text{Mg(OH)}_2$  was added into the mixture in order to promote the growth of single crystals and the  $\text{MgO}$  proportion in the starting materials was slightly adjusted accordingly. The mixture was loaded into a platinum capsule 2 mm in diameter and 3 mm in length. This assemblage was then compressed to 20 GPa and heated at 1600 °C for 1 hr, and then cooled to 1300 °C keeping for 2 hrs (RUN #: 5K2283).

For the  $^{57}\text{Fe}$ -bearing NAL sample, the starting materials was prepared using the same procedure for the Fe-free sample, but

10 mol% of the  $\text{Al}_2\text{O}_3$  in the starting materials was substituted by  $^{57}\text{Fe}_2\text{O}_3$  (>95% enrichment in  $^{57}\text{Fe}$ ). The NAL phase has been reported to contain 6–12 mol% iron according to previous studies using natural MORB composition (Ricolleau et al., 2010). The lower bound of the iron content in the NAL phase (~6 mol%) has been chosen for preparing this starting sample assemblage used for the high pressure–temperature synthesis of the crystal in this study. The sample assemblage was compressed to 24 GPa and then heated to 1400 °C for 24 hrs (RUN #: 5K2420). Analysis of the recovered Fe-bearing NAL phase shows ~5 mol% iron ( $\text{Fe}^{2+}$  and  $\text{Fe}^{3+}$ ) in the lattice, consistent with our original estimate for the sample synthesis (see further discussion for the chemical analysis below).

Microscope observations of the recovered samples from the capsules showed euhedral single crystals approximately 50–200  $\mu\text{m}$  in diameter with hexagonal prism shape, and that the Fe-free NAL crystals are colorless while the Fe-bearing NAL crystals are bluish. Electron microprobe analysis (EMPA) of the crystals revealed that both samples are chemically homogeneous. The Fe-free crystal has a chemical composition of  $\text{Na}_{1.14}\text{Mg}_{1.83}\text{Al}_{4.74}\text{Si}_{1.23}\text{O}_{12}$  (12 oxygen atoms per formula). Single-crystal XRD measurements indicated that the synthesized crystals are in the hexagonal NAL phase structure with a space group of  $P6_3/m$ . The refined lattice parameters for the Fe-free NAL phase at ambient conditions are  $a = b = 8.736(5)$  Å,  $c = 2.770(1)$  Å, and  $V = 183.1(1)$  Å<sup>3</sup> with a density of 3.86 g/cm<sup>3</sup>, consistent with literature values (Guignot and Andraut, 2004; Imada et al., 2012). A traditional Mössbauer spectrum (MS) of the Fe-bearing sample was collected at ambient conditions using a  $^{57}\text{Co}$  in Rh point source in transmission geometry at the Bayerisches Geoinstitut, Universität Bayreuth. The spectrum was analyzed using the program MossA (Prescher et al., 2012). Analysis of the MS showed three doublets of iron in the Fe-bearing NAL phase, one assigned to  $\text{Fe}^{2+}$  and two  $\text{Fe}^{3+}$ , with a  $\text{Fe}^{3+}/\Sigma\text{Fe}$  ratio of 0.64(15) (Fig. S2). The derived hyperfine parameters are as follows (isomer shifts are relative to  $\alpha$ -Fe):  $\text{Fe}^{2+}$  (Doublet 1) with quadrupole splitting (QS) = 3.07(13) mm/s and isomer shift (IS) = 1.10(7) mm/s,  $\text{Fe}^{3+}$  (Doublet 2) with QS = 0.78(14) mm/s and IS = 0.55(15) mm/s, and  $\text{Fe}^{3+}$  (Doublet 3) with QS = 0.60(6) mm/s and IS = 0.27(3) mm/s. According to the combined results from EMPA, XRD, and MS analyses, the  $^{57}\text{Fe}$ -enriched NAL phase has a chemical composition of  $\text{Na}_{0.71}\text{Mg}_{2.05}\text{Al}_{4.62}\text{Si}_{1.16}\text{Fe}^{2+}_{0.09}\text{Fe}^{3+}_{0.17}\text{O}_{12}$  with refined lattice parameters of  $a = b = 8.762(4)$  Å,  $c = 2.7789(8)$  Å, and  $V = 184.76(6)$  Å<sup>3</sup> at ambient conditions. Unpolarized infrared spectra of the NAL phase were measured and analyzed to constrain its  $\text{H}_2\text{O}$  content using an iN10-type Fourier Transform spectrometer at Peking University (Fig. S4). The integral molar absorption coefficient of nepheline ( $\text{NaAlSi}_3\text{O}_8$ ) was employed to calculate the  $\text{H}_2\text{O}$  content of the NAL phase by means of the Beer–Lambert law (Bell et al., 2003; Beran and Rossman, 1989). The Fe-free NAL phase contains 0.1 wt%  $\text{H}_2\text{O}$ . For the Fe-bearing NAL, the single-crystal size is too small to measure high signal-to-noise spectra. Since the starting materials for synthesis of the Fe-bearing NAL are the same as those of the Fe-free NAL counterpart except for 5.5 wt%  $\text{Fe}_2\text{O}_3$  substitution for  $\text{Al}_2\text{O}_3$ , we thus assume that the water content in these crystals should be similar to each other. The relatively low water content of 0.1 wt% in the crystals is not expected to significantly influence high-pressure elastic parameters as well as spin states of iron reported here.

## 2.2. Nuclear forward scattering

NFS experiments were performed at the 16-ID-D beamline of HPCAT at the Advanced Photon Source (APS), Argonne National Laboratory (ANL). A monochromatic X-ray beam of ~14.4125 keV

with 2.2 meV energy resolution and a beam size 20  $\mu\text{m}$  in diameter was used to excite  $^{57}\text{Fe}$  nuclei in the sample to observe nuclear resonance. Time-delayed spectra were recorded by an avalanche photodiode detector in the forward direction. The collection time for each NFS spectrum was 3–4 hrs. Two runs of NFS experiments were performed employing two symmetric-type DACs. The first run of NFS experiments were carried out up to 42 GPa using a DAC equipped with diamond anvil culets of 400  $\mu\text{m}$  in diameter. In the second run, another DAC with anvil culets of 200  $\mu\text{m}$  in diameter was used to perform the NFS experiments up to 86 GPa. Rhenium gaskets were pre-indented to approximately 20 GPa, and holes with about half of the culet diameter were drilled and subsequently used as the sample chambers. A piece of double-side polished single-crystal plate of the Fe-bearing NAL phase was loaded into the sample chamber for each run, together with a few ruby spheres for pressure calibration and neon as the pressure medium. Pressures were measured from the ruby fluorescence spectra before and after each NFS collection to determine pressure uncertainty of each pressure step (Mao et al., 1986). XRD patterns of the sample were collected at high pressure to confirm its crystal structure. All of the NFS spectra were evaluated using the CONUSS program to derive hyperfine parameters of iron ions in the lattice (Sturhahn, 2000).

## 2.3. Single-crystal X-ray diffraction

High-pressure single-crystal XRD experiments were performed at the 13-ID-D beamline of the GSECARS at the APS, using a monochromatic X-ray beam with a wavelength of 0.3344 Å and a beam size of ~3  $\mu\text{m}$  (FWHM). Two short symmetric type DACs equipped with diamond culets of 200  $\mu\text{m}$  diameter were used for these experiments. Rhenium gaskets were pre-indented to approximately 25 GPa with a thickness of ~25  $\mu\text{m}$ . A hole of 90  $\mu\text{m}$  in diameter was drilled in the pre-indented gasket and used as the sample chamber for each run experiments. Two double-side polished single-crystal platelets, one for the Fe-free NAL phase and the other for the Fe-bearing NAL phase, were loaded into each of the sample chambers, together with fine platinum powder as the pressure calibrant for XRD experiments (Fei et al., 2007), a few ruby spheres for pressure calibration in gas loading (Mao et al., 1986), and neon as the pressure medium. High-pressure single-crystal XRD experiments were performed up to about 82 GPa at approximately 1 GPa pressure intervals. The diffraction patterns were recorded with an exposure duration of 10 s, during which the DAC on the sample stage was rotated with an angle of  $\pm 10^\circ$  about the vertical axis of the DAC holder.

Spotty diffraction peaks of the single-crystal diffraction patterns were evaluated to obtain  $d$  spacing values using the software packages GSE\_ADA (Dera et al., 2013). The obtained  $d$  spacings were indexed to Miller indices (hkl) according to the known structure file of the NAL phase (Miura et al., 2000). Lattice parameters were then derived from the refinement of  $d_{hkl}$  spacings using the program Unitcell (Holland and Redfern, 1997). The indexed single-crystal diffraction patterns of the Fe-free NAL phase at 1.7 GPa and 82.0 GPa are shown in Fig. S3. Analysis of the peak width of the diffraction spots indicates that the high quality of the single-crystal NAL phase was maintained up to the maximum pressure in the present experiments (Fig. S3(b)).

## 3. Results and discussion

### 3.1. Spin and valence states of iron in the NAL phase

Analysis of the MS at ambient conditions shows three doublets of the iron ions in the NAL structure (Fig. S2). Based on the derived hyperfine parameters and reference hyperfine parameters for

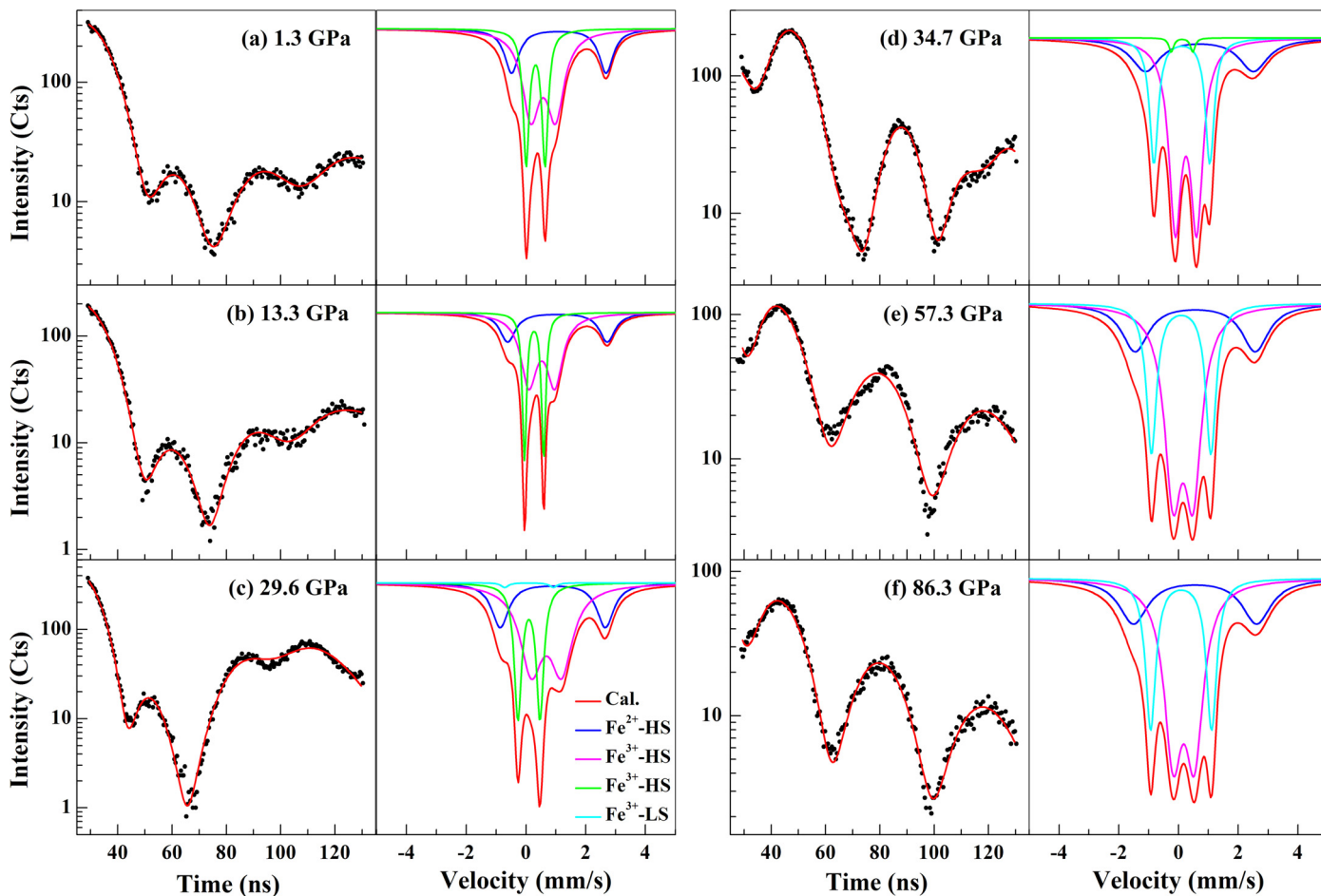
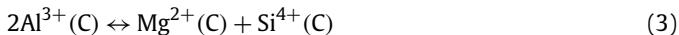
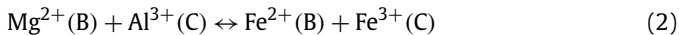


**Fig. 1.** Representative nuclear forward scattering spectra of the Fe-bearing NAL phase (chemical composition:  $\text{Na}_{0.71}\text{Mg}_{2.05}\text{Al}_{4.62}\text{Si}_{1.16}\text{Fe}^{2+}_{0.09}\text{Fe}^{3+}_{0.17}\text{O}_{12}$ ) at high pressures. Corresponding energy spectra calculated from the fitting results of the NFS spectra are shown in the right panels. All but the spectra at 29.6 and 34.7 GPa were modeled with three iron doublets. The spectra at 29.6 and 34.7 GPa were modeled with a four-doublet model in which both HS and LS  $\text{Fe}^{3+}$  were considered within the spin transition region. Black dots: experimental NFS spectra; red lines: modeled spectra; blue lines: high-spin  $\text{Fe}^{2+}$  in the B site (Doublet 1); magenta lines: high-spin  $\text{Fe}^{3+}$  in the B site (Doublet 2); green lines: high-spin  $\text{Fe}^{3+}$  in the C site (Doublet 3); cyan lines: low-spin  $\text{Fe}^{3+}$  in the C site (Doublet 3). (For interpretation of the references to color in this figure legend, the reader is referred to the web version of this article.)

rock-forming minerals (Burns, 2005; Dyar et al., 2006), the doublet with an extremely high QS of 3.07 mm/s can be assigned to high-spin  $\text{Fe}^{2+}$  (Doublet 1), whereas other two doublets (Doublet 2 and Doublet 3) with relatively low QS represent high-spin  $\text{Fe}^{3+}$ . These site assignments of the three doublets in the NAL phase can be reconciled with its crystal structure. The NAL phase has a general formula of  $\text{AB}_2\text{C}_6\text{O}_{12}$  ( $P6_3/m$ ,  $Z = 1$ ), where A represents a large monovalent or divalent cation ( $\text{K}^+$ ,  $\text{Na}^+$ , or  $\text{Ca}^{2+}$ ) in the hexagonal tunnel, B represents a medium-sized cation ( $\text{Mg}^{2+}$ ,  $\text{Fe}^{2+}$ , or  $\text{Fe}^{3+}$ ) in the trigonal prismatic site, and C is in the octahedral site occupied by a small cation ( $\text{Mg}^{2+}$ ,  $\text{Al}^{3+}$ ,  $\text{Si}^{4+}$ , or  $\text{Fe}^{3+}$ ) (Fig. S1) (Miura et al., 2000). There are four substitution mechanisms proposed for an ideal  $\text{CaMg}_2\text{Al}_6\text{O}_{12}$ :



leading to a complex chemical formula reported previously for the NAL phase (Miura et al., 2000; Miyajima et al., 2001; Pamato et al., 2014). The cations in the six-fold coordinated environment of the trigonal prismatic B and the octahedral C sites have ionic radii:  $R(\text{Mg}^{2+}) = 0.860 \text{ \AA}$ ,  $R(\text{Si}^{4+}) = 0.540 \text{ \AA}$ ,  $R(\text{Al}^{3+}) = 0.675 \text{ \AA}$ ,  $R(\text{Fe}^{2+}\text{-HS}) = 0.920 \text{ \AA}$ , and  $R(\text{Fe}^{3+}\text{-HS}) = 0.785 \text{ \AA}$  (Shannon, 1976).

$\text{Fe}^{2+}$ , with an ionic radius similar to  $\text{Mg}^{2+}$ , prefers to occupy the B site, whereas  $\text{Fe}^{3+}$  occupies both B and C sites. Based on the crystal field theory,  $\text{Fe}^{3+}$  with the trigonal prismatic coordination has a larger electric field gradient and a higher crystal field splitting energy than that in the octahedral coordination (Burns, 2005; Hoffmann et al., 1976), leading to a higher QS. Thus, doublet 1 with a high QS of 3.07 mm/s is assigned to be the high-spin  $\text{Fe}^{2+}$  in the B site, doublet 2 with QS = 0.78 mm/s and IS = 0.55 mm/s is assigned to be the high-spin  $\text{Fe}^{3+}$  in the B site, and doublet 3 with QS = 0.6 mm/s and IS = 0.27 mm/s represents the high-spin  $\text{Fe}^{3+}$  in the C site (Fig. S2).

### 3.2. Spin transition of $\text{Fe}^{3+}$ in the NAL phase at high pressure

NFS spectra of the Fe-bearing NAL phase were collected up to 86 GPa at pressure intervals of approximately 4 GPa (Fig. 1). The spectra below 30 GPa show three quantum beats that do not change significantly with increasing pressure. At pressures above 30 GPa, however, the locations and intensities of the quantum beats in the spectra change dramatically indicating an electronic transition of iron in the Fe-bearing NAL phase. Beyond 35 GPa, no further major change was observed in the spectra. On the basis of the traditional MS results at ambient conditions, the NFS spectra at  $P < 25 \text{ GPa}$  and  $P > 35 \text{ GPa}$  were fitted sufficiently using a three-doublet model, one for  $\text{Fe}^{2+}$  and two for  $\text{Fe}^{3+}$ , respectively, but the spectra at  $25 \text{ GPa} < P < 35 \text{ GPa}$  were fitted using a four-

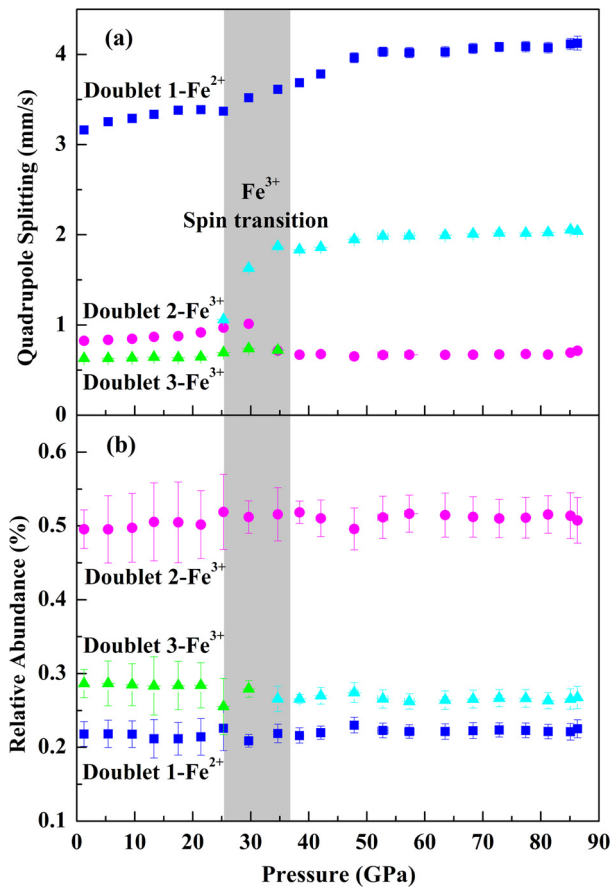


**Fig. 2.** Derived quadrupole splitting (a) and relative abundance (b) of three doublets for  $\text{Fe}^{2+}$  and  $\text{Fe}^{3+}$  in the Fe-bearing NAL phase at high pressures. Doublet 1 (blue squares) is assigned to the high-spin  $\text{Fe}^{2+}$  in the B site. Doublet 2 (magenta circles) represents the high-spin  $\text{Fe}^{3+}$  in the B site, whereas Doublet 3 (green triangles for the high-spin state and cyan triangles for the low-spin state) is the  $\text{Fe}^{3+}$  in the C site. Gray shaded region represents the spin transition region of the octahedral  $\text{Fe}^{3+}$  (Doublet 3). The colors of symbols in this figure correspond to the colors of lines for three doublets in the Fig. 1 and Fig. S2. (For interpretation of the references to color in this figure legend, the reader is referred to the web version of this article.)

doublet model (Fig. 1). The derived hyperfine parameters of the three doublets at 1.3 GPa are consistent with the traditional MS results (Table S1). The derived  $\text{Fe}^{3+}/\Sigma\text{Fe}$  ratio from NFS is 0.78(5) at 1.3 GPa, which is higher than 0.64(15) from the MS results at ambient conditions. These values are consistent within the expected uncertainties, since the intensity of each contribution varies between time-domain spectra compared to energy-domain spectra, and the  $\text{Fe}^{2+}$  absorption in the energy-domain spectrum is relatively broad (Fig. S2).

The derived hyperfine parameters of the three iron doublets are plotted in Fig. 2 and listed in Table S1. The QS values of each doublet increase smoothly with increasing pressure below 30 GPa, which can be ascribed to the enhanced lattice distortion of the iron site in the NAL phase with increasing pressure (Burns, 2005; Dyar et al., 2006). At pressures between 25 and 35 GPa, the QS of  $\text{Fe}^{3+}$  in the octahedral C site (Doublet 3) dramatically increases from 0.7 to 1.86 mm/s, while QS values of  $\text{Fe}^{2+}$  (Doublet 1) and  $\text{Fe}^{3+}$  (Doublet 2) in the B site slightly increase and decrease, respectively (Fig. 2(a)). Literature results for the pressure effects on the hyperfine parameters of  $\text{Fe}^{3+}$  and  $\text{Fe}^{2+}$  ions in oxides and silicates show that an electronic HS-to-LS transition of the octahedral  $\text{Fe}^{3+}$  is typically associated with an increase in the QS value, while the spin transition of the octahedral  $\text{Fe}^{2+}$  can lead to a disappearance of the QS (Lin et al., 2012; McCammon et al., 2010). For example, the  $\text{Fe}^{3+}$  spin transition in the octahedral site of bridg-

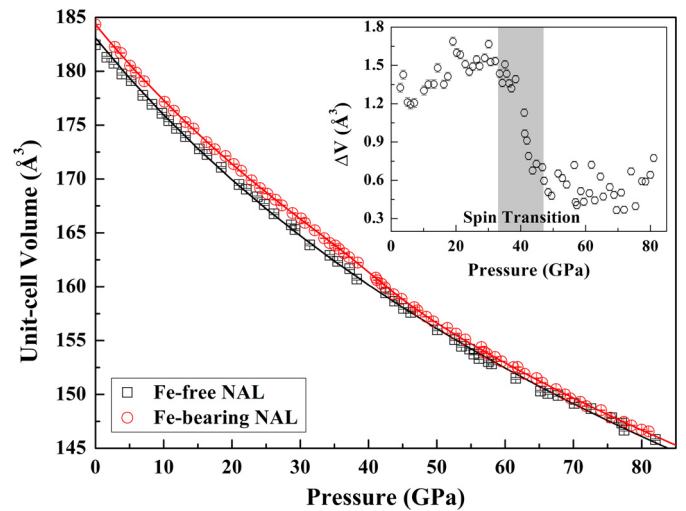


**Fig. 3.** Unit-cell volumes for the Fe-free NAL (black squares) and Fe-bearing NAL (red cycles) phase as a function of pressure. The inserted figure shows the volume differences ( $\Delta V$ ) between the Fe-free and the Fe-bearing NAL phase as a function of pressure. Open circles: experimental results; solid lines: modeled results using the 2nd-order Birch–Murnaghan equation of state and the method from Wentzcovitch et al. (2009). Gray shaded region represents the spin transition zone of  $\text{Fe}^{3+}$  in the octahedral site. (For interpretation of the references to color in this figure legend, the reader is referred to the web version of this article.)

manite causes a significant increase in QS from 0.65 to 2 mm/s between 13 and 24 GPa (Lin et al., 2012). We can thus attribute the significant increase in the QS of the doublet 3 to a  $\text{Fe}^{3+}$  spin transition in the octahedral site of the NAL phase occurring at approximately 30 GPa. On the other hand, the  $\text{Fe}^{3+}$  spin transition in the octahedral site likely causes a change in the local atomic site configurations, resulting in an increase in the QS of  $\text{Fe}^{2+}$  in the B site (Doublet 1) from 3.42 to 3.67 mm/s, and a slight decrease in the QS of  $\text{Fe}^{3+}$  in the B site (Doublet 2) from 0.97 to 0.7 mm/s (Fig. 2(a)). This observation of the enhanced QS value of  $\text{Fe}^{2+}$  in the NAL phase is similar to the extremely high QS values of  $\text{Fe}^{2+}$  observed in the pseudo-dodecahedral site of bridgmanite that can reach to as high as approximately 4 mm/s (Jackson et al., 2005; Lin et al., 2012). We note that  $\text{Fe}^{2+}$  in the B site of the NAL phase exhibits a high QS value of 3.07 mm/s even at ambient conditions, similar to the high QS values observed in Fe-bearing pyrope garnet (Mao et al., 2013), indicating an extremely large electric field gradient of the local environment of iron as a result of a large lattice distortion of the coordination polyhedron in the B site. At pressures above 50 GPa, the QS of each doublet increases monotonically and slowly with increasing pressure, indicating an increasing resistance of the lattice against further distortion (Fig. 2(a)). It should be noted that the relative abundance of each doublet remains unchanged within the experimental uncertainties at pressures up to 86 GPa, suggesting that applied pressure does not induce any electronic charge exchange between  $\text{Fe}^{2+}$  and  $\text{Fe}^{3+}$  iron ions in the NAL phase (Fig. 2(b)).

### 3.3. Equation of state of the NAL phase

The unit-cell parameters of the two NAL phase crystals at high pressures are listed in Tables S2 and S3, and their unit-cell volumes are plotted in Fig. 3. The unit-cell volume of the Fe-free NAL phase varies smoothly with increasing pressure and the pressure–volume ( $P$ – $V$ ) data are fitted to the Birch–Murnaghan equation of state (B–M EoS). For the 3rd-order B–M EoS modeling, the fit yields: the unit-cell volume at zero pressure  $V_0 = 183.1(1) \text{ \AA}^3$ , the isothermal bulk modulus  $K_{T0} = 233(6) \text{ GPa}$  and its pressure derivative  $K'_{T0} = 3.7(2)$ . Using the 2nd-order B–M EoS, the fit

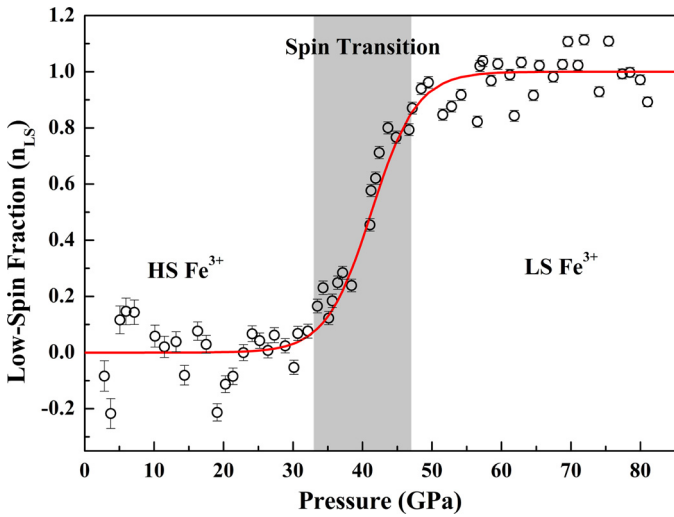


**Fig. 4.** Low-spin fraction ( $n_{LS}$ ) of the octahedral  $Fe^{3+}$  in the Fe-bearing NAL phase as a function of pressure. Open circles: experimental results; red line: modeled results. Gray shaded region represents spin transition zone of the octahedral  $Fe^{3+}$ . The modeled results are derived using the method reported by Wentzcovitch et al. (2009). (For interpretation of the references to color in this figure legend, the reader is referred to the web version of this article.)

yields  $K_{T0} = 224(2)$  GPa with a fixed  $K'_{T0} = 4$ . The derived EoS parameters for the Fe-free NAL phase are in good agreement with literature values (Imada et al., 2012; Kato et al., 2013). However, compared to the  $P$ - $V$  curve of the Fe-free NAL, the  $P$ - $V$  curve of the Fe-bearing NAL shows a volume discontinuity at approximately 33 GPa. To further identify the pressure range of the volume discontinuity and evaluate the effect of the iron substitution on the incompressibility of the NAL phase, we have calculated the volume differences between the Fe-bearing and Fe-free NAL samples at high pressures, which show a dramatic volume reduction of  $1.2 \text{ \AA}^3$  (approximately 1.0%) maximum at pressures 33–47 GPa (Fig. 3 insert). Since the pressure region of this volume reduction coincides with the spin transition pressure of the octahedral  $Fe^{3+}$  in the NFS measurements, this volume discontinuity can be attributed to the spin transition of octahedral  $Fe^{3+}$  in the Fe-bearing NAL phase.

According to the spin transition zone of 33–47 GPa derived from the volume reduction (Fig. 3),  $P$ - $V$  data at pressures <28 GPa and >56 GPa were selected for the high-spin and low-spin states of the Fe-bearing NAL phase, respectively, to avoid the coexistence of HS and LS states in the vicinity of the spin transition region. A 2nd-order B-M EoS with a fixed  $K'_{T0} = 4$  has been used to fit the  $P$ - $V$  data of the Fe-bearing NAL phase, yielding:  $V_{0-HS} = 184.76(6) \text{ \AA}^3$  and  $K_{T0-HS} = 238(1)$  GPa for the HS state;  $V_{0-LS} = 183.8(5) \text{ \AA}^3$  and  $K_{T0-LS} = 226(5)$  GPa for the LS state (Fig. 3). The derived  $V_0$ ,  $K_{T0}$  and  $K'_{T0}$  of the HS and LS states for the Fe-bearing NAL are in good agreement with results of the Fe-free NAL, indicating that substitution of iron only causes a volume increase and does not significantly affect the EoS parameters. With the derived EoS parameters of the HS and LS states, we obtained the LS fraction ( $n_{LS}$ ) at high pressure (Fig. 4). The mixed-spin state of the Fe-bearing NAL phase within the spin crossover region was treated as an ideal solid solution of the HS and LS states with the volume relation (Wentzcovitch et al., 2009):

$$V = n_{LS}V_{LS} + (1 - n_{LS})V_{HS} \quad (5)$$

where  $V_{HS}$  and  $V_{LS}$  are the unit cell volumes of the HS and LS states, respectively. The experimentally calculated  $n_{LS}$  of the Fe-bearing NAL phase at high pressures were modeled using the methods reported previously (Fig. 4) (Wentzcovitch et al., 2009):

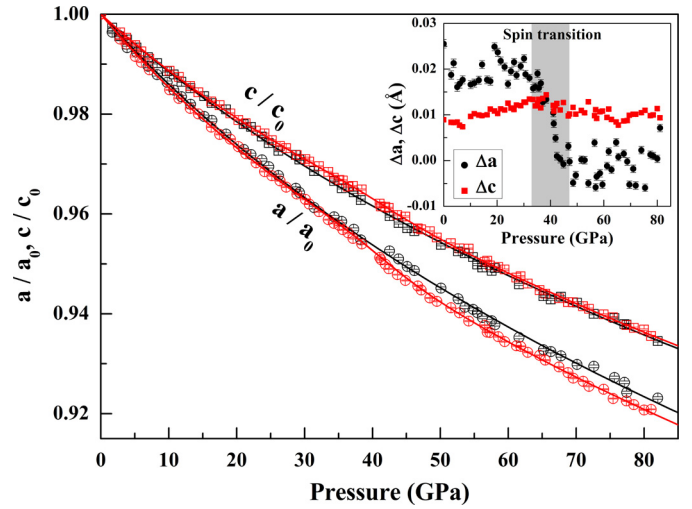


**Fig. 5.** Normalized unit-cell lattice parameters with respect to their room pressure values ( $a/a_0$  and  $c/c_0$ ) for the Fe-free NAL (black) and Fe-bearing NAL (red) phase as a function of pressure. The inserted figure is the axial length differences ( $\Delta a$  and  $\Delta c$ ) between the Fe-bearing and Fe-free NAL phase at high pressures. Open symbols: experimental results; solid lines: modeled results. The modeled results are derived from the fits of the modified Birch-Murnaghan equation of state to the compression curve using the low-spin fraction (Xia et al., 1998; Wentzcovitch et al., 2009). Gray shaded region represents spin transition zone of the octahedral  $Fe^{3+}$ . (For interpretation of the references to color in this figure legend, the reader is referred to the web version of this article.)

$$n_{LS} = \frac{1}{1 + \exp\left(\frac{\Delta G_{LS-HS}}{T}\right)} \quad (6)$$

$$\Delta G_{LS-HS} = b_0 + b_1 \frac{P - P_{HS}}{P_{LS} - P_{HS}} \quad (7)$$

where  $\Delta G_{LS-HS}$  is the difference in the Gibbs free energy of the LS and HS states,  $b_0$  and  $b_1$  are temperature-dependent constants ( $b_0 = -546(55)$  K and  $b_1 = 1186(105)$  K in this study), and  $P_{LS}$  and  $P_{HS}$  are the beginning pressure of the LS state and the ending pressure of the HS state, respectively. This model has been successfully employed to derive the spin fractions of iron in candidate lower-mantle minerals using experimental  $P$ - $V$ - $T$  data (Chang et al., 2013; Liu et al., 2014; Mao et al., 2011). As shown in Fig. 4, for the LS fraction of the Fe-bearing NAL phase as a function of pressure, the spin transition zone ranges from approximately 33 to 47 GPa with a width of 14 GPa. The pressure region of the spin transition determined from XRD is larger than that from NFS. This difference may be due to different sensitivities of the techniques: NFS is a more sensitive technique to detect changes in the local iron environments, while XRD is used to probe lattice planes for derivation of the unit-cell volumes.

### 3.4. Axial incompressibility

To investigate the effect of iron on the axial incompressibility of the NAL phase, the normalized unit-cell lattice parameters ( $a/a_0$  and  $c/c_0$ ) with respect to their ambient values for the two NAL samples are plotted for comparison (Fig. 5). No visible discontinuity was observed in the  $a/a_0$  and  $c/c_0$  of the Fe-free NAL phase up to the maximum pressure of 82 GPa. The lattice parameters,  $a$  and  $c$ , of the Fe-free NAL phase as a function of pressure were fitted using a modified form of the 3rd-order B-M EoS (Xia et al., 1998):

$$P = \frac{3}{2}K_{l0} \left[ \left( \frac{l_0}{l} \right)^7 - \left( \frac{l_0}{l} \right)^5 \right] \left\{ 1 + \frac{3}{4}(K'_{l0} - 4) \left[ \left( \frac{l_0}{l} \right)^2 - 1 \right] \right\} \quad (8)$$

where  $l_0$  and  $l$  are the lattice parameters  $a$  or  $c$  at zero pressure and high pressure, respectively,  $K_{l0}$  is the axial incompressibility,

and  $K'_{I0}$  is the pressure derivative of  $K_{I0}$ . The fits of the present axial compression data yield:  $a_0 = 8.736(5)$  Å and  $K_{a0} = 219(6)$  GPa with  $K'_{a0} = 3.6(2)$ ;  $c_0 = 2.770(1)$  Å and  $K_{c0} = 269(8)$  GPa with  $K'_{c0} = 4.0(2)$ . Compared to the Fe-free NAL phase,  $c/c_0$  of the Fe-bearing NAL phase decreases smoothly with increasing pressure, but  $a/a_0$  shows a slight reduction at pressures 33~40 GPa corresponding to the Fe<sup>3+</sup> spin transition zone (Fig. 5). To further identify the effect of iron on the axial incompressibility of the NAL phase, the differences in the lattice parameters ( $\Delta a$  and  $\Delta c$ ) between the Fe-bearing and Fe-free NAL phase were calculated using the experimental data of the Fe-bearing sample and the modeled values from the EoS of the Fe-free NAL (Fig. 5 insert). The derived  $\Delta a$  data show a dramatic reduction at around 33~47 GPa, corresponding to the HS-to-LS transition zone revealed in the analysis of the NFS spectra and in the volume reduction region from XRD data, however, no discontinuity was observed for the  $\Delta c$  data. Thus, the volume discontinuity caused by the spin transition of the octahedral Fe<sup>3+</sup> in the NAL phase appears to result almost entirely from a shortening of the  $a$ -axis at 33~47 GPa.

The NAL phase exhibits obvious anisotropy in the axial compressibility with the  $a$ -axis more compressible than the  $c$ -axis (Fig. 5), and this behavior can be understood from its crystal structure (Fig. S1). The AlO<sub>6</sub>, SiO<sub>6</sub>, or FeO<sub>6</sub> octahedra of the NAL phase are joined via sharing edges parallel to the  $c$ -axis to form a chain framework structure, and adjacent chains share edges and corners perpendicular to the  $c$ -axis to form two kinds of tunnels with hexagonal and di-trigonal cross sections (Fig. S1) (Miura et al., 2000). When pressure is applied to the NAL phase, the  $a$ -axis direction has large tunnel space that can be compressed by both compressing and rotating octahedra. Nevertheless, the  $c$ -axis direction with the chain structure shows greater resistance than the  $a$ -axis direction to compression of the stiff octahedral chains. In the NAL phase, the octahedra are more sensitive to the applied pressure than the trigonal prisms, thus, applied pressure can induce the spin transition of Fe<sup>3+</sup> in the octahedral C site more easily than Fe<sup>2+</sup> and Fe<sup>3+</sup> in the trigonal prismatic B site. Future studies on the single-crystal elasticity of the NAL phase using Brillouin light scattering are needed to elucidate the lattice and acoustic anisotropy of the NAL phase across the spin transition at high pressures.

### 3.5. Incompressibility and bulk sound velocity across the spin transition

Based on the derived EoS parameters and the low spin fractions, the isothermal bulk modulus ( $K_T$ ) and bulk sound velocity ( $V_\phi$ ) of the NAL phase were calculated using the following equations (Fig. 6) (Wentzcovitch et al., 2009):

$$\frac{V}{K_T} = n_{LS} \frac{V_{LS}}{K_{T-LS}} + (1 - n_{LS}) \frac{V_{HS}}{K_{T-HS}} - (V_{LS} - V_{HS}) \left( \frac{\partial n_{LS}}{\partial P} \right)_T \quad (9)$$

$$V_\phi = \sqrt{\frac{K}{\rho}} \quad (10)$$

where  $K_{T-HS}$  and  $K_{T-LS}$  are the bulk moduli of the HS and LS states at high pressures, respectively, and  $\rho$  is the density. The bulk modulus of the Fe-free NAL phase increases smoothly with increasing pressure, while  $K_T$  of the Fe-bearing NAL phase shows significant elastic softening in the spin transition region with a maximum softening of 17.6% at 41 GPa (Fig. 6(a)).

To evaluate the geophysical consequences of the observed elastic softening of the NAL phase in subducted slabs, the bulk moduli of other major candidate minerals of the MORB assemblage in the lower mantle, including Fe, Al-bearing bridgmanite (FeAl-Pv), CaSiO<sub>3</sub> perovskite (Ca-Pv), stishovite (St) and CaCl<sub>2</sub>-type SiO<sub>2</sub> phases, were also evaluated and plotted for comparison with that

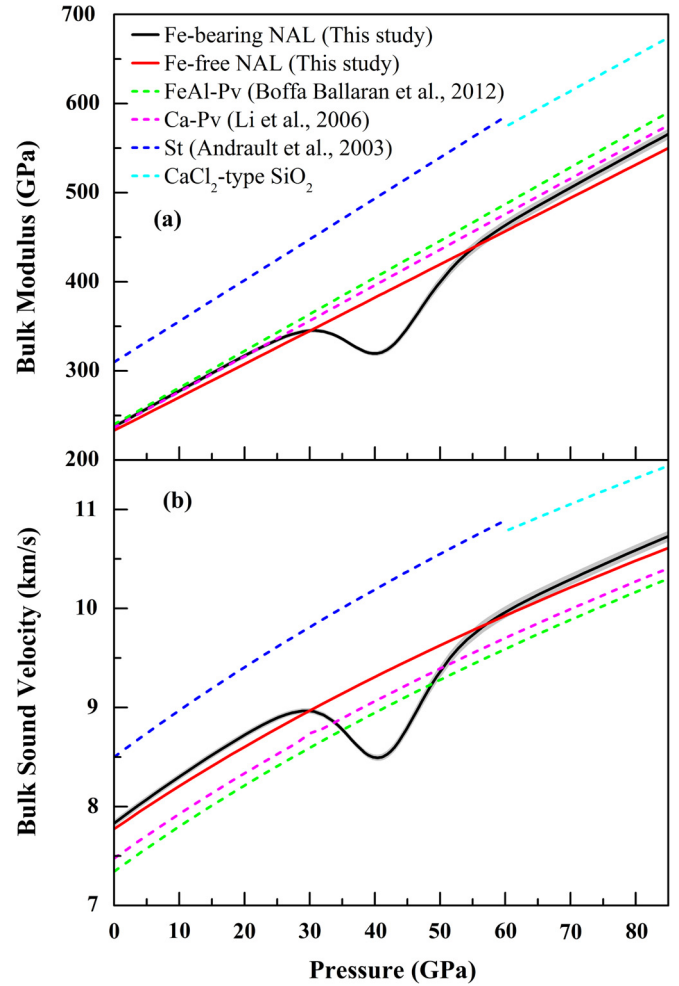


**Fig. 6.** Isothermal bulk moduli ( $K_T$ ) and bulk sound velocities ( $V_\phi$ ) of the Fe-free NAL (red) and Fe-bearing NAL (black) phase at high pressures. Gray shaded regions stand for the uncertainties of  $K_T$  and  $V_\phi$  on the Fe-bearing NAL phase.  $K_T$  and  $V_\phi$  of other major candidate minerals of the subducted MORB assemblage in the lower mantle are also plotted in dashed lines for comparison. FeAl-Pv (green); Fe, Al-bearing bridgmanite (Boffa Ballaran et al., 2012); Ca-Pv (magenta); CaSiO<sub>3</sub> perovskite (Li et al., 2006); St (blue); stishovite and CaCl<sub>2</sub>-type SiO<sub>2</sub> (cyan) (Andraut et al., 2003). (For interpretation of the references to color in this figure legend, the reader is referred to the web version of this article.)

of the NAL phase (Andraut et al., 2003; Boffa Ballaran et al., 2012; Li et al., 2006). Without considering the spin crossover, the bulk moduli of the NAL phase are slightly smaller than those of FeAl-Pv and Ca-Pv (Fig. 6(a)). Stishovite and CaCl<sub>2</sub>-type SiO<sub>2</sub> have significantly higher bulk moduli than other candidate phases. The bulk sound velocities of the NAL phase, FeAl-Pv, Ca-Pv, St and CaCl<sub>2</sub>-type SiO<sub>2</sub> are shown in Fig. 6(b) (Andraut et al., 2003; Boffa Ballaran et al., 2012; Li et al., 2006). In the experimental pressure range except for the spin transition region, bulk sound velocities of the NAL phase are higher than those of FeAl-Pv and Ca-Pv by approximately 6%, but lower than those of St and CaCl<sub>2</sub>-type SiO<sub>2</sub>. Therefore, the potential presence of the NAL phase with a content up to 30 wt% in the MORB assemblage can contribute to a relatively higher bulk sound velocity profile in the lower mantle. Additionally, the spin transition of the octahedral Fe<sup>3+</sup> in the Fe-bearing NAL phase is associated with a softening of  $V_\phi$ , reaching a maximum softening of 9.4% at 41 GPa and 300 K (Fig. 6(b)).

## 4. Implications

Seismological studies have indicated the presence of seismic heterogeneities, such as seismic discontinuities and reflectors, or

scatterers, at lower-mantle depths beneath the western Pacific subduction zones (Castle and van der Hilst, 2003; Kaneshima, 2013; Kaneshima and Helffrich, 2009; Kawakatsu and Niu, 1994; Vanacore et al., 2006; Vinnik et al., 2001). The mid-mantle seismic discontinuities were characterized beneath subduction zones of Pacific regions (Kawakatsu and Niu, 1994; Vinnik et al., 2001), and the seismic scatterers or reflectors characterized by the S-to-P converted wave range from 660 to 1800 km depth (Castle and van der Hilst, 2003; Kaneshima, 2013; Kaneshima and Helffrich, 2009; Niu et al., 2003; Vanacore et al., 2006). Amplitude and waveform analyses from short-period seismic wave data suggested a decrease in shear wave velocity by 2~6% within the seismic reflector at a depth of ~1115 km (Niu et al., 2003). The observed seismic heterogeneities in the lower mantle are generally suggested to be related to the presence of subducted slabs. The seismic heterogeneities in the mid-lower mantle have been attributed to the presence of basalt, which contains free-silica phases ( $\text{SiO}_2$ ) that are seismically fast (Fig. 6(b)) (Bina, 2010), and the second-order phase transition of  $\text{SiO}_2$  from stishovite to the  $\text{CaCl}_2$ -type structure could produce a softening with velocity anomalies large enough to be seismically detectable at ~1500 km (Carpenter et al., 2000). However, three other plausible explanations for the seismic heterogeneities in the shallow lower mantle (depths <1000 km) were proposed based on mantle dynamics studies, such as remnants of ancient basaltic crustal materials, dehydration reactions of dense hydrous magnesium silicate phases, and the sharp boundary between fine-grained isotropic rocks and coarse-grained anisotropic rocks (Kaneshima, 2013).

The velocity softening of the NAL phase associated with the  $\text{Fe}^{3+}$  spin transition observed here may provide a new insight into seismic observations of subducted slabs in the lower mantle. In this study, the spin transition of the octahedral  $\text{Fe}^{3+}$  in the NAL phase occurs at approximately 30~47 GPa corresponding to pressures of the lower mantle. Two sets of experimental results, namely the change in  $^{57}\text{Fe}$  NFS spectra and the volume discontinuity of the Fe-bearing NAL phase, independently support the  $\text{Fe}^{3+}$  spin transition in the NAL phase at high pressure. Using the EoS parameters of the Fe-free and Fe-bearing NAL phase in this study, the bulk sound velocity-profiles of a MORB assemblage has been calculated at three given temperatures of 300 K, 800 K, and 1200 K, respectively, in the upper-to-middle parts of the lower mantle (Fig. 7). The volume proportions of the constituent minerals in the MORB assemblage considered here are 40% FeAl-Pv, 20% Ca-Pv, 20% St, and 20% NAL (Ricolleau et al., 2010), in which the NAL phase is assumed to be the only Al-rich phase. The  $V_\phi$  profiles of the MORB-1 assemblage at 300 K, 800 K, and 1200 K were calculated from these candidate phases containing the Fe-free NAL phase, while the MORB-2 assemblage at 300 K represents the ones including the Fe-bearing NAL. The velocity profile of PREM was also plotted for comparison (Dziewonski and Anderson, 1981). Thermoelastic parameters of the candidate minerals in the MORB assemblage used for these modeling are listed in Table S4 (Supplementary material). Our modeled results show that the bulk sound velocities of the MORB-1 assemblage at 1200 K are consistently larger than that of PREM by 0.2~0.4 km/s. The inserted figure in Fig. 7 shows the  $V_\phi$  difference between MORB-1 and MORB-2 ( $(V_{\phi\text{-MORB-2}} - V_{\phi\text{-MORB-1}}) / V_{\phi\text{-MORB-1}} \times 100\%$ ) at 300 K, which displays a sharp reduction of 1.8% maximum at ~41 GPa resulting from the  $\text{Fe}^{3+}$  spin transition of the Fe-bearing NAL phase observed in this study. Assuming that the HT effect on the spin transition of the NAL phase is similar to that of ferropericlase (Mao et al., 2011), the onset pressure for the LS state will increase by ~10 GPa from 300 K to 1200 K and the width of the spin transition zone will expand from ~15 GPa to ~25 GPa at 1200 K. The  $V_\phi$  reduction associated with the spin crossover of the NAL phase in the MORB-2 assemblage at 1200 K

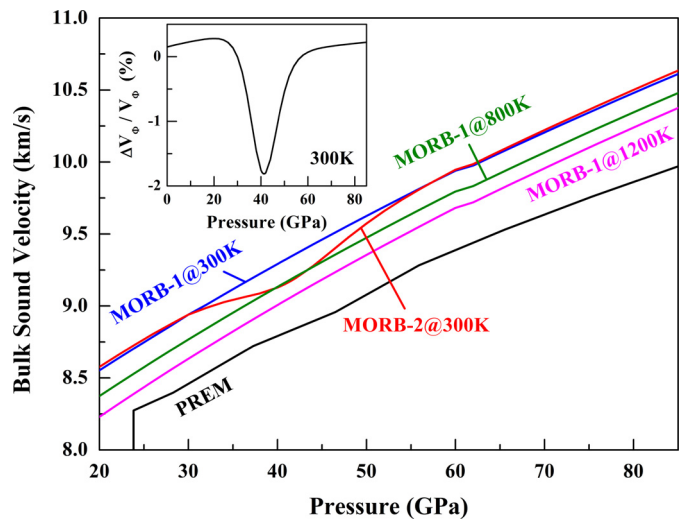


Fig. 7. Bulk sound velocity profiles ( $V_\phi$ ) of a subducted MORB assemblage as a function of pressure at three representative temperatures of 300 K, 800 K, and 1200 K. The volume proportions of the constituent minerals in the MORB assemblage considered here are 40% FeAl-Pv, 20% Ca-Pv, 20% St, and 20% NAL (Ricolleau et al., 2010), in which the NAL phase is assumed to be the only Al-rich phase. The  $V_\phi$  profiles of the MORB-1 at 300 K, 800 K, and 1200 K were calculated from these candidate phases containing the Fe-free NAL phase, while the MORB-2 at 300 K represents the ones including the Fe-bearing NAL. The velocity profile of PREM was also plotted for comparison (Dziewonski and Anderson, 1981). The inserted figure shows the  $V_\phi$  difference between MORB-1 and MORB-2 ( $(V_{\phi\text{-MORB-2}} - V_{\phi\text{-MORB-1}}) / V_{\phi\text{-MORB-1}} \times 100\%$ ) at 300 K.

is thus expected to occur at pressures higher than 41 GPa but with a significant reduced magnitude. We should note that the Fe-bearing NAL phase contains ~5 mol% iron ( $\text{Fe}^{2+}$  and  $\text{Fe}^{3+}$ ) in this study, where ~1.5 mol%  $\text{Fe}^{3+}$  in octahedral site undergoes HS to LS transition. The NAL phase is reported to contain up to ~12 mol% iron according to previous studies on natural MORB composition (Ricolleau et al., 2010). Such a high proportion of iron in the NAL phase, having potential spin transitions of iron at high pressure, can give rise to more distinct velocity softening than those results presented in this study. The NAL phase is reported to be stable at P-T conditions relevant to the shallow parts of the lower-mantle (depths  $\leq$  1200 km) (Ricolleau et al., 2010; Walter et al., 2011). Therefore, the distinct elastic properties of the NAL phase associated with the octahedral  $\text{Fe}^{3+}$  spin transition suggest that it may provide an alternative plausible explanation for the observed seismic heterogeneities of subducted slabs in the lower mantle at depths below 1200 km.

Application of high temperature to a system with a spin transition is known to provide higher configuration entropy to stabilize the mixed-spin state (Tsuchiya et al., 2006), such that the width of the spin transition is expanded and the onset pressure for occurrence of the LS state is increased at higher temperatures. For example, the width of the spin transition occurring in ferropericlase is ~15 GPa at 300 K, but expands to ~25 GPa at 1200 K. The onset pressure for the LS state increases from ~50 GPa at 300 K to 65 GPa at 1200 K (Mao et al., 2011). Therefore, the velocity softening associated with the spin transition is expected to be broaden and reduced at high P-T conditions. The effect of temperature on the spin transition of the NAL phase and then the elastic properties of subducted basaltic crust should be considered in future studies. Since the NAL phase is expected to transform to the CF phase at pressures above 50 GPa, and that the CF phase is expected to contain up to 20 mol% iron (Ricolleau et al., 2010), further studies on the effect of the spin transition of the NAL and CF phases on seismic velocities, rheology and chemistry are also needed to decipher the behavior and properties of subducted MORB assemblage in the lower mantle.

## 5. Conclusions

In summary, we have observed an electronic HS to LS transition of the octahedral Fe<sup>3+</sup> in the Fe-bearing NAL phase at pressures ranging from 30 to 47 GPa. The Fe<sup>2+</sup> and Fe<sup>3+</sup> in the trigonal prism B site remain in the HS state at all pressures of this study. The spin transition is associated with a volume reduction of approximately 1% ( $\sim 1.2 \text{ \AA}^3$ ), resulting almost entirely from the shortening of the *a*-axis. The NAL phase exhibits strong anisotropic axial incompressibility, and the *a*-axis is much more compressible than the *c*-axis. The spin transition results in significant softening in the bulk modulus by a maximum reduction of 17.6% and the bulk sound velocity by a maximum reduction of 9.4%. Comparing our results with other candidate minerals in subducted slabs in the lower mantle, the bulk sound velocity of the NAL phase is  $\sim 6\%$  higher than those of Fe, Al-bearing bridgmanite and Ca–Pv in the lower-mantle pressures except for the spin transition zone. These distinct elastic properties of the NAL phase observed in this study can be used to understand the observed seismic heterogeneities in the lower mantle.

## Acknowledgements

We thank J. Liu and J. Yang for experimental assistance and helpful discussion, X. Liu for infrared spectra measurements, and W.L. Bi for her help with the use of the CONUSS. X. Wu acknowledges financial support from the National Science Foundation of China (U1232204 and 41473056). J.F. Lin acknowledges financial support from the US National Science Foundation Geophysics Program and Deep Carbon Observatory (DCO). High-pressure experiments were performed at HPCAT and GeoSoilEnviroCARS of the APS, ANL. HPCAT operations are supported by DOE–NNSA under Award No. DE–NA0001974 and DOE–BES under Award No. DE–FG02–99ER45775. GeoSoilEnviroCARS operations are supported by the National Science Foundation–Earth Sciences (EAR–1128799) and the Department of Energy, Geosciences (DE–FG02–94ER14466). APS is supported by DOE–BES, under Contract No. DE–AC02–06CH11357.

## Appendix A. Supplementary material

Supplementary material related to this article can be found online at <http://dx.doi.org/10.1016/j.epsl.2015.11.011>.

## References

- Akaogi, M., Hamada, Y., Suzuki, T., Kobayashi, M., Okada, M., 1999. High pressure transitions in the system MgAl<sub>2</sub>O<sub>4</sub>–CaAl<sub>2</sub>O<sub>4</sub>: a new hexagonal aluminous phase with implication for the lower mantle. *Phys. Earth Planet. Inter.* 115, 67–77.
- Andraut, D., Angel, R.J., Mosenfelder, J.L., Le Bihan, T., 2003. Equation of state of stishovite to lower mantle pressures. *Am. Mineral.* 88, 301–307.
- Bell, D.R., Rossman, G.R., Maldener, J., Endisch, D., Rauch, F., 2003. Hydroxide in olivine: a quantitative determination of the absolute amount and calibration of the IR spectrum. *J. Geophys. Res., Solid Earth* (1978–2012) 108, 2105.
- Beran, A., Rossman, G., 1989. The water content of nepheline. *Mineral. Petrol.* 40, 235–240.
- Bina, C.R., 2010. Scale limits of free-silica seismic scatterers in the lower mantle. *Phys. Earth Planet. Inter.* 183, 110–114.
- Bina, C., Helffrich, G., 2014. Geophysical constraints on mantle composition. In: *Treatise on Geochemistry*, pp. 41–65.
- Boffa Ballaran, T., Kurnosov, A., Glazyrin, K., Frost, D.J., Merlini, M., Hanfland, M., Caracas, R., 2012. Effect of chemistry on the compressibility of silicate perovskite in the lower mantle. *Earth Planet. Sci. Lett.* 333, 181–190.
- Burns, R.G., 2005. *Mineralogical Applications of Crystal Field Theory*. Cambridge University Press.
- Carpenter, M.A., Hemley, R.J., Mao, H., 2000. High-pressure elasticity of stishovite and the P<sub>4</sub>/mmn  $\rightleftharpoons$  Pnnm phase transition. *J. Geophys. Res.* 105, 10807–10816.
- Castle, J.C., van der Hilst, R.D., 2003. Searching for seismic scattering off mantle interfaces between 800 km and 2000 km depth. *J. Geophys. Res., Solid Earth* (1978–2012) 108, 2095.
- Chang, Y.Y., Jacobsen, S.D., Lin, J.F., Bina, C.R., Thomas, S.M., Wu, J., Shen, G., Xiao, Y., Chow, P., Frost, D.J., McCammon, C.A., Dera, P., 2013. Spin transition of Fe<sup>3+</sup> in Al-bearing phase D: an alternative explanation for small-scale seismic scatterers in the mid-lower mantle. *Earth Planet. Sci. Lett.* 382, 1–9.
- Dai, L., Kudo, Y., Hirose, K., Murakami, M., Asahara, Y., Ozawa, H., Ohishi, Y., Hirao, N., 2013. Sound velocities of Na<sub>0.4</sub>Mg<sub>0.6</sub>Al<sub>1.6</sub>Si<sub>0.4</sub>O<sub>4</sub> NAL and CF phases to 73 GPa determined by Brillouin scattering method. *Phys. Chem. Miner.* 40, 195–201.
- Dera, P., Zhuravlev, K., Prakash, V., Rivers, M.L., Finkelstein, G.J., Grubor-Urošević, O., Tschauer, O., Clark, S.M., Downs, R.T., 2013. High pressure single-crystal micro X-ray diffraction analysis with GSE\_ADA/RSV software. *High Press. Res.* 33, 466–484.
- Dyar, M.D., Agresti, D.G., Schaefer, M.W., Grant, C.A., Sklute, E.C., 2006. Mössbauer spectroscopy of earth and planetary materials. *Annu. Rev. Earth Planet. Sci.* 34, 83–125.
- Dziewonski, A.M., Anderson, D.L., 1981. Preliminary reference Earth model. *Phys. Earth Planet. Inter.* 25, 297–356.
- Fei, Y., Ricolleau, A., Frank, M., Mibe, K., Shen, G., Prakapenka, V., 2007. High-pressure geosience special feature: toward an internally consistent pressure scale. *Proc. Natl. Acad. Sci.* 104, 9182–9186.
- Fukao, Y., Obayashi, M., Nakakuki, T., 2009. Stagnant slab: a review. *Annu. Rev. Earth Planet. Sci.* 37, 19–46.
- Green, D., Hiberson, W., Jaques, A., 1979. Petrogenesis of mid-ocean ridge basalts, the Earth: its origin. In: *Structure and Evolution*. Academic Press, London, pp. 265–299.
- Guignot, N., Andraut, D., 2004. Equations of state of Na–K–Al host phases and implications for MORB density in the lower mantle. *Phys. Earth Planet. Inter.* 143–144, 107–128.
- Hirose, K., Takafuji, N., Sata, N., Ohishi, Y., 2005. Phase transition and density of subducted MORB crust in the lower mantle. *Earth Planet. Sci. Lett.* 237, 239–251.
- Hoffmann, R., Howell, J.M., Rossi, A.R., 1976. Bicapped tetrahedral, trigonal prismatic, and octahedral alternatives in main and transition group six-coordination. *J. Am. Chem. Soc.* 98, 2484–2492.
- Hofmann, A., 1997. Mantle geochemistry: the message from oceanic volcanism. *Nature* 385, 219–229.
- Holland, T.J.B., Redfern, S.A.T., 1997. Unit cell refinement from powder diffraction data: the use of regression diagnostics. *Mineral. Mag.* 61, 65–77.
- Imada, S., Hirose, K., Ohishi, Y., 2011. Stabilities of NAL and Ca–ferrite-type phases on the join NaAlSiO<sub>4</sub>–MgAl<sub>2</sub>O<sub>4</sub> at high pressure. *Phys. Chem. Miner.* 38, 557–560.
- Imada, S., Hirose, K., Komabayashi, T., Suzuki, T., Ohishi, Y., 2012. Compression of Na<sub>0.4</sub>Mg<sub>0.6</sub>Al<sub>1.6</sub>Si<sub>0.4</sub>O<sub>4</sub> NAL and Ca–ferrite-type phases. *Phys. Chem. Miner.* 39, 525–530.
- Irfune, T., Ringwood, A., 1993. Phase transformations in subducted oceanic crust and buoyancy relationships at depths of 600–800 km in the mantle. *Earth Planet. Sci. Lett.* 117, 101–110.
- Jackson, J.M., Sturhahn, W., Shen, G., Zhao, J., Hu, M.Y., Errandonea, D., Bass, J.D., Fei, Y., 2005. A synchrotron Mössbauer spectroscopy study of (Mg, Fe)SiO<sub>3</sub> perovskite up to 120 GPa. *Am. Mineral.* 90, 199–205.
- Kaneshima, S., 2013. Lower mantle seismic scatterers below the subducting Tonga slab: evidence for slab entrainment of transition zone materials. *Phys. Earth Planet. Inter.* 222, 35–46.
- Kaneshima, S., Helffrich, G., 2009. Lower mantle scattering profiles and fabric below Pacific subduction zones. *Earth Planet. Sci. Lett.* 282, 234–239.
- Kato, C., Hirose, K., Komabayashi, T., Ozawa, H., Ohishi, Y., 2013. NAL phase in K-rich portions of the lower mantle. *Geophys. Res. Lett.* 40, 5085–5088.
- Kawai, K., Tsuchiya, T., 2012. Phase stability and elastic properties of the NAL and CF phases in the NaMg<sub>2</sub>Al<sub>5</sub>SiO<sub>12</sub> system from first principles. *Am. Mineral.* 97, 305–314.
- Kawakatsu, H., Niu, F., 1994. Seismic evidence for a 920-km discontinuity in the mantle. *Nature* 371, 301–305.
- Li, L., Weidner, D.J., Brodholt, J., Alfe, D., David Price, G., Caracas, R., Wentzcovitch, R., 2006. Elasticity of CaSiO<sub>3</sub> perovskite at high pressure and high temperature. *Phys. Earth Planet. Inter.* 155, 249–259.
- Lin, J.F., Struzhkin, V.V., Jacobsen, S.D., Hu, M.Y., Chow, P., Kung, J., Liu, H., Mao, H.K., Hemley, R.J., 2005. Spin transition of iron in magnesiowüstite in the Earth's lower mantle. *Nature* 436, 377–380.
- Lin, J.F., Alp, E.E., Mao, Z., Inoue, T., McCammon, C., Xiao, Y., Chow, P., Zhao, J., 2012. Electronic spin states of ferric and ferrous iron in the lower-mantle silicate perovskite. *Am. Mineral.* 97, 592–597.
- Lin, J.F., Speziale, S., Mao, Z., Marquardt, H., 2013. Effects of the electronic spin transitions of iron in lower mantle minerals: implications for deep mantle geophysics and geochemistry. *Rev. Geophys.* 51, 244–275.
- Liu, J., Lin, J.F., Mao, Z., Prakapenka, V.B., 2014. Thermal equation of state and spin transition of magnesioferrite at high pressure and temperature. *Am. Mineral.* 99, 84–93.
- Mao, H.K., Xu, J., Bell, P.M., 1986. Calibration of the ruby pressure gauge to 800-kbar under quasi-hydrostatic conditions. *J. Geophys. Res.* 91, 4673–4676.
- Mao, Z., Lin, J.F., Liu, J., Prakapenka, V.B., 2011. Thermal equation of state of lower-mantle ferropervicite across the spin crossover. *Geophys. Res. Lett.* 38, L23308.

- Mao, Z., Lin, J.F., Huang, S., Chen, J., Xiao, Y., Chow, P., 2013. Synchrotron Mössbauer study of Fe-bearing pyrope at high pressures and temperatures. *Am. Mineral.* 98, 1146–1152.
- McCammon, C., Dubrovinsky, L., Narygina, O., Kantor, I., Wu, X., Glazyrin, K., Sergeev, I., Chumakov, A., 2010. Low-spin Fe<sup>2+</sup> in silicate perovskite and a possible layer at the base of the lower mantle. *Phys. Earth Planet. Inter.* 180, 215–221.
- Miura, H., Hamada, Y., Suzuki, T., Akaogi, M., Miyajima, N., Fujino, K., 2000. Crystal structure of CaMg<sub>2</sub>Al<sub>6</sub>O<sub>12</sub>, a new Al-rich high pressure form. *Am. Mineral.* 85, 1799–1803.
- Miyajima, N., Fujino, K., Funamori, N., Kondo, T., Yagi, T., 1999. Garnet–perovskite transformation under conditions of the Earth's lower mantle: an analytical transmission electron microscopy study. *Phys. Earth Planet. Inter.* 116, 117–131.
- Miyajima, N., Yagi, T., Hirose, K., Kondo, T., Fujino, K., Hiroyuki, M., 2001. Potential host phase of aluminum and potassium in the Earth's lower mantle. *Am. Mineral.* 86, 740–746.
- Niu, F., Kawakatsu, H., Fukao, Y., 2003. Seismic evidence for a chemical heterogeneity in the midmantle: a strong and slightly dipping seismic reflector beneath the Mariana subduction zone. *J. Geophys. Res., Solid Earth (1978–2012)* 108, 2419.
- Ohta, K., Hirose, K., Lay, T., Sata, N., Ohishi, Y., 2008. Phase transitions in pyrolite and MORB at lowermost mantle conditions: implications for a MORB-rich pile above the core–mantle boundary. *Earth Planet. Sci. Lett.* 267, 107–117.
- Ono, A., Akaogi, M., Kojitani, H., Yamashita, K., Kobayashi, M., 2009. High-pressure phase relations and thermodynamic properties of hexagonal aluminous phase and calcium–ferrite phase in the systems NaAlSiO<sub>4</sub>–MgAl<sub>2</sub>O<sub>4</sub> and CaAl<sub>2</sub>O<sub>4</sub>–MgAl<sub>2</sub>O<sub>4</sub>. *Phys. Earth Planet. Inter.* 174, 39–49.
- Pamato, M.G., Kurnosov, A., Ballaran, T.B., Trots, D.M., Caracas, R., Frost, D.J., 2014. Hexagonal Na<sub>0.41</sub>[Na<sub>0.125</sub>Mg<sub>0.79</sub>Al<sub>0.085</sub>]<sub>2</sub>[Al<sub>0.79</sub>Si<sub>0.21</sub>]<sub>6</sub>O<sub>12</sub> (NAL phase): crystal structure refinement and elasticity. *Am. Mineral.* 99, 1562–1569.
- Prescher, C., McCammon, C., Dubrovinsky, L., 2012. MossA: a program for analyzing energy-domain Mössbauer spectra from conventional and synchrotron sources. *J. Appl. Crystallogr.* 45, 329–331.
- Ricolleau, A., Perrillat, J.P., Fiquet, G., Daniel, I., Matas, J., Addad, A., Menguy, N., Cardon, H., Mezouar, M., Guignot, N., 2010. Phase relations and equation of state of a natural MORB: implications for the density profile of subducted oceanic crust in the Earth's lower mantle. *J. Geophys. Res.* 115, B08202.
- Shannon, R.D., 1976. Revised effective ionic radii and systematic studies of interatomic distances in halides and chalcogenides. *Acta Crystallogr., Sect. A* 32, 751–767.
- Sturhahn, W., 2000. CONUSS and PHOENIX: evaluation of nuclear resonant scattering data. *Hyperfine Interact.* 125, 149–172.
- Sun, S.S., 1982. Chemical composition and origin of the Earth's primitive mantle. *Geochim. Cosmochim. Acta* 46, 179–192.
- Tsuchiya, T., Wentzcovitch, R.M., da Silva, C.R., de Gironcoli, S., 2006. Spin transition in magnesiowüstite in Earth's lower mantle. *Phys. Rev. Lett.* 96, 198501.
- Vanacore, E., Niu, F., Kawakatsu, H., 2006. Observations of the mid-mantle discontinuity beneath Indonesia from S to P converted waveforms. *Geophys. Res. Lett.* 33, L04302.
- Vinnik, L., Kato, M., Kawakatsu, H., 2001. Search for seismic discontinuities in the lower mantle. *Geophys. J. Int.* 147, 41–56.
- Walter, M.J., Kohn, S.C., Araujo, D., Bulanova, G.P., Smith, C.B., Gaillou, E., Wang, J., Steele, A., Shirey, S.B., 2011. Deep mantle cycling of oceanic crust: evidence from diamonds and their mineral inclusions. *Science* 334, 54–57.
- Wentzcovitch, R.M., Justo, J.F., Wu, Z., da Silva, C.R.S., Yuen, D.A., Kohlstedt, D., 2009. Anomalous compressibility of ferropericlase throughout the iron spin cross-over. *Proc. Natl. Acad. Sci.* 106, 8447–8452.
- Xia, X., Weidner, D.J., Zhao, H., 1998. Equation of state of brucite: single-crystal Brillouin spectroscopy study and polycrystalline pressure–volume–temperature measurement. *Am. Mineral.* 83, 68–74.
- Yamada, H., Matsui, Y., Eiji, I., 1983. Crystal–chemical characterization of NaAlSiO<sub>4</sub> with the CaFe<sub>2</sub>O<sub>4</sub> structure. *Mineral. Mag.* 47, 177–181.